National Aeronautics and Space Administration

Orbital Debris Quarterly News

Volume 24, Issue 3
August 2020

Inside...

A publication of the NASA Orbital Debris Program Office (ODPO)

International Space Station Maneuvers to Avoid Debris

The International Space Station (ISS) conducted two maneuvers to avoid potential collisions with large debris tracked by the U.S. Space Command (USSPACECOM) Space Surveillance Network (SSN) on 19 April and 3 July.

The maneuver in April was triggered by a high-risk conjunction with a breakup fragment generated from the *Fengyun-1C* (*FY-1C*) anti-satellite test conducted by China in 2007. That fragment has an International Designator of 1999-025BNN and an SSN Catalog ID of 31280. Because of the conjunction's timing, the ISS Program used the opportunity of a planned deboost maneuver (to set up the proper orbit configuration for upcoming ISS visiting vehicles) to also avoid the high-risk conjunction with the *FY-1C* debris.

The July maneuver was to avoid an object with International Designator 1987-079AG and SSN# 27923, which was generated from the explosion of a *SOZ* (*Sistema Obespecheniya Zapuska*, "Launch Support System") ullage motor, or SL-12 auxiliary motor, in 2003. A total of 42 fragments from the explosion of that *SOZ* motor (International Designator 1987-079H, SSN# 18375) are large enough to catalog, including object 27923. Due to a design flaw, more than 50 *SOZ* ullage-motor explosions have been documented so far.

The ISS has conducted a total of 27 collision avoidance maneuvers since 1999. The avoided objects included two *FY-1C* debris and five debris from the 2009 collision between Cosmos 2251 and Iridium 33 (two from the former and three from the latter). In addition, there was a high-risk conjunction between the ISS and NASA's operational Global Precipitation Measurement (GPM) spacecraft in 2017, and the GPM spacecraft maneuvered to mitigate the risk of collision.

The history of the ISS collision avoidance maneuvers, the number of SSN-tracked, ISS-orbit-crossing objects, and the solar activity for F10.7 cm flux are shown in the figure on page 2. The number of the SSN-tracked, ISS-orbit-crossing objects is influenced by several factors, including space traffic and debris population, solar activity, and the altitude of the ISS, which varied between approximately 320 km and 430 km over the years. The frequency of the ISS collision avoidance maneuvers is affected by the ISS conjunction risk mitigation protocol, the number of the ISS-orbit-crossing objects, and the accuracy of conjunction assessments. The latter depends on sensor capability, data processing and analysis, and solar activity. Under the leadership of the 18th Space Control Squadron, the accuracy of object tracking and conjunction assessments has improved in recent years.

Orbital debris has been identified as a major safety risk for the ISS with respect to loss of mission and loss of crew. The U.S. modules on the ISS are well-protected against impacts by small orbital debris. The protective shields are effective against orbital debris about 1 cm and smaller. The objects shown as circles in the figure are large enough to be tracked by the SSN, which are objects approximately 10 cm and larger. Collision risk against such large objects can be mitigated by conjunction assessments and collision avoidance maneuvers when necessary. Therefore, the biggest threat to the U.S. modules on the ISS comes from orbital debris between 1 cm and 10 cm. Since the orbital debris population follows a power-law size distribution, meaning there is a higher number of small debris than large debris, the risk to the U.S. modules is actually driven by orbital debris in the 1 cm–2 cm range. The number of such small debris crossing the ISS orbit is about 20 times greater than the blue circles shown in the figure. Other non-U.S. modules on the ISS are not as well protected against small orbital debris impacts. The risk to those modules is driven by sub-centimeter orbital debris. ♦

see figure on page 2

ISS Maneuvers

continued from page 2

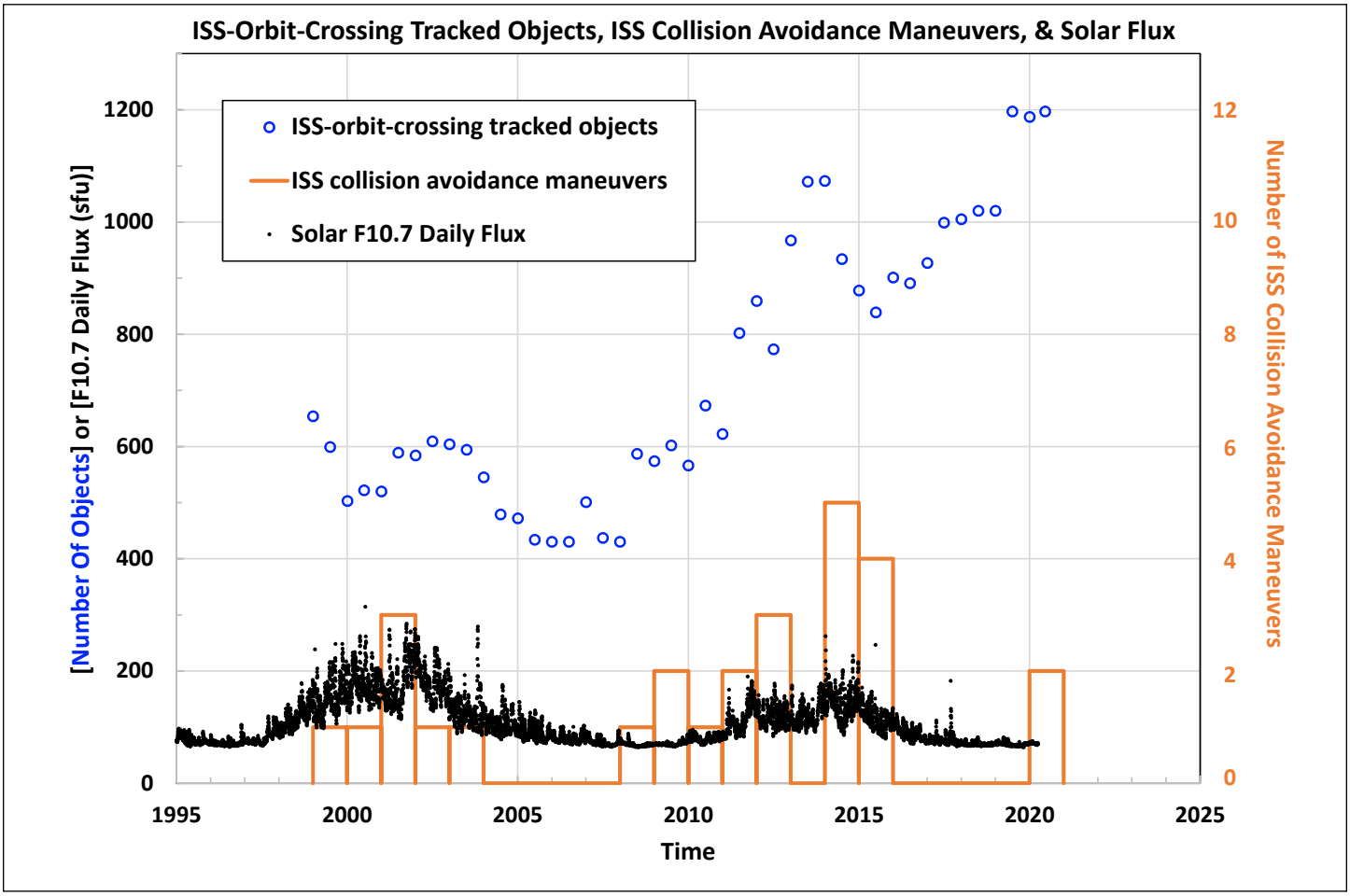

Number of the ISS-orbit-crossing objects tracked by the SSN (blue circles), the solar F10.7 daily flux (black dots), and the history of the ISS collision avoidance maneuvers (orange histogram).

Second Fragmentation of *Fregat* Upper Stage Debris

A debris object associated with the launch of Russia's *Spektr-R* radio astronomy satellite fragmented on 8 May 2020 between 0402 GMT and 0551 GMT. The object (International Designator 2011-037B, U.S. Space Command Space Surveillance Network [SSN] catalog number 37756) had experienced a prior breakup event, of unknown cause, in August 2015.

Previously described in the SSN catalog as "SL-23 DEB," the object is now identified as "FREGAT DEB (TANK)". The Lavochkin *Fregat-SB* used in this launch is based on the *Fregat* upper stage but adds a toroidal hypergolic fuel/oxidizer tank, the *sbrasyvaemye blok bakov* (*SBB*) and variously referred to as the jettisoned tanks unit (JTU) or block (JTB). The reader is referred to the previous ODQN news article (ODQN, vol. 20, Issues 1 & 2 joint issue, pp. 2-3*) for detailed illustrations and a description of the physical attributes of the vehicle, including stored energy and possible failure modes.

At the time of the May 2020 event, the *SBB* was in a 3606 x 422 km-altitude, 51.5° inclination orbit. It had been on-orbit for approximately 4.0 years and 8.8 years at the respective times of the two events.

A total of 24 fragments were initially tracked from the August 2015 event. As of 5 June 2020, however, none had been confirmed and cataloged. The May 2020 event produced approximately 65 tracked debris of which 36, including the parent body, had entered the catalog by 5 June. The 2011-037 debris ensemble of the parent body (piece tag B) and new debris (piece tags H through AT, inclusive) are portrayed in the figure's Gabbard diagram (shown on pg. 3).

While the presence of residual stored energy, particularly the hypergolic propellants, offers a likely root cause of this energetic event, uncertainties associated with actual construction details render the actual cause unknown at this time. ♦

* Note: The ODQN article's second reference, "Propulsion System for Delivering "Phobos-Grunt" Spacecraft on Phobos Surface," is now identified as having been authored by Yu.G. Stekolshchikov, S.S. Stepanov, L.G. Alexandrov, and V.P. Makarov of the Lavochkin Association.

see figure on page 3

Fregat Fragmentation

continued from page 2

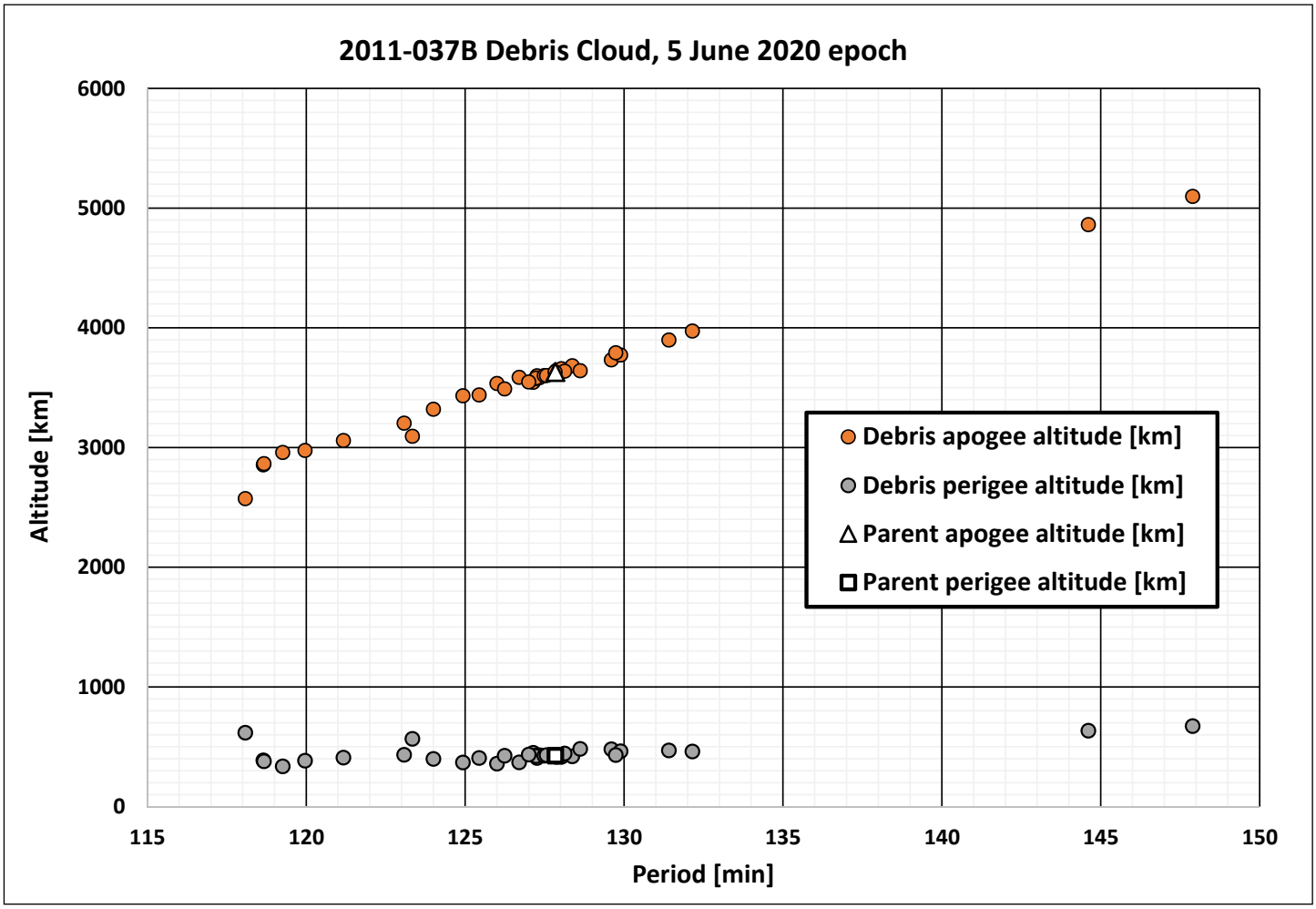

A Gabbard diagram of the 8 May 2020 2011-037B event. Approximate epoch is 5 June 2020. The maximum change in period is approximately 20 minutes, and the maximum change in inclination is 0.21°.

Debris Assessment Software Version 3.1 Release

The Orbital Debris Program Office has released version 3.1 of the Debris Assessment Software (DAS), replacing the prior October 2019 release of DAS 3.0. The updated version provides data that can verify compliance of a spacecraft, upper stage, and/or payload with NASA's requirements for limiting debris generation, spacecraft vulnerability, postmission lifetime, and entry safety.

This release incorporates an update to the Orbital Debris Engineering Model (ORDEM), version 3.1, which was unveiled in ODQN, vol. 24, issue 1, p. 3. Another change to DAS is the removal of the Grün meteoroid flux model. To calculate penetration risk from meteoroids, users should consult the NASA Meteoroid Environment Office and Hypervelocity Impact Technology teams for assessments.

Successful verification of a design in DAS demonstrates compliance with NASA debris mitigation requirements. Historically, DAS analysis has proven acceptable in meeting compliance requirements of many other agencies in the U.S. and around the world. It does not address the inherent design reliability facets of NASA requirements, but addresses all Earth-related orbital debris requirements that make up the bulk of the requirements in the NASA Technical Standard 8719.14B.

For new users, DAS is available for download, by permission only, and requires that an application be completed via the NASA Software Catalog. To begin the process, click on the Request Now! button in the catalog at https://software.nasa.gov/software/MSC-26690-1 .

Users who have already completed the software request process for earlier versions of DAS 3.x do not need to reapply for DAS 3.1. Simply go to your existing account on the NASA Software portal and download the latest installer. Approval for DAS is on a per project basis: approval encompasses activities and personnel working within the project scope identified in the application. ♦

PROJECT REVIEW

The Development of Experimental Hypervelocity Impact Capabilities with Non-Spherical Projectiles

J. MILLER, B. DAVIS, T. JUDD, AND R. MCCANDLESS
(HYPERVELOCITY IMPACT TECHNOLOGY GROUP)
A. DELGADO, D. HENDERSON, A. PARDO,
D. RODRIGUEZ, AND M. SANDY
(REMOTE HYPERVELOCITY TEST LABORATORY)

In 2014 a laboratory impact experiment, DebriSat, was conducted at Arnold Engineering Development Center. A still frame image series of the experiment is shown in Figure 1 [1, 2]. DebriSat was designed to replicate a catastrophic impact to update the NASA satellite breakup model and to support the development of a fragment shape distribution for the future Orbital Debris Engineering Model (ORDEM 4.0), which will improve the fidelity of orbital debris impact risk assessments [2, 3]. To this end, DebriSat was built with many modern materials including structural panels of carbon-fiber reinforced polymer (CFRP).

Subsequent to the experiment, DebriSat fragments were extracted from porous catcher foam panels that minimized secondary damage to the debris during the capture process [3, 4]. Thus far, one of the key observations is that CFRP fragments represent a large fraction of the collected debris and that these fragments tend to be thin, "flake-like" structures or long, "needle-like" structures, as illustrated in Figure 1; whereas, debris with nearly equal dimensions is less prevalent. As current ballistic-limit models for shields are based upon spherical impacting particles [5], the DebriSat experiment has pointed to a missing component in the current approach to ballistic modeling that must be considered. To improve risk assessments of spacecraft design reliability and survivability, refined, broad-ranging, non-spherical ballistic limit equations are needed to prepare for the future Bumper implementation of ORDEM 4.0. This effort is funded by the NASA HQ Office of Safety and Mission Assurance (OSMA).

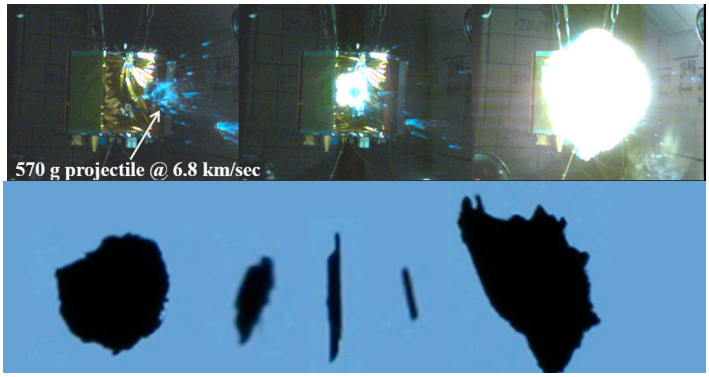

Figure 1. The DebriSat experiment subjected a representative modern satellite to a hypervelocity impact (top) of a 570 g-aluminum projectile at 6.8 km/s, which resulted in the catastrophic break-up of the satellite. A large database of debris was captured and is being categorized with a large portion of the debris being (bottom) carbon-fiber reinforced polymer with shapes from large and flat "flake-like" objects to long and thin "needle-like" objects. Credit: (top) Arnold Engineering Development Complex/United States Air Force; (bottom) University of Florida, Dept. of Mechanical & Aerospace Engineering, Space Systems Group.

While numerous shield types are currently in use for impact mitigation from orbital debris and meteoroids, the most common shield in use is the double-wall shield commonly known as a Whipple shield [6]. This shield achieves a high level of ballistic performance for minimal weight because the stresses induced in a projectile during impact are far above the stresses the solid particle can withstand, resulting in a break-up of the particle. In the Whipple shield approach, an empty volume between the two walls of the shield provides a space for the debris cloud to expand, resulting in a distributed impact on the second shield-wall; however, even with the increased performance of this design, the shield-wall reaches a limit, which is the ballistic-limit of the shield-system [7].

The pure, all-metal, Whipple shield is less prevalent in deployment due to operational thermal environments [5]. A previous ODQN article, (ODQN, vol. 22, issue 4, November 2018, pp. 2-4), [8] developed a numerical simulation model of a representative International Space Station (ISS) shield with the material configuration shown in Figure 2. This shield carries a higher risk of penetration than most other ISS shields due to its lower ballistic capability, and therefore, its performance is of particular interest to the operation of the ISS.

This numerical simulation model was executed over a broad range of impact conditions to capture the effect of the non-spherical nature of the debris collected from DebriSat. However, accounting for geometric properties, like material thicknesses, separation, and orientation, is not sufficient to address potential concerns with material constitutive properties in a numerical simulation model. To ensure that modeling of the material constitutive properties has been performed properly, a collection of impact validation data is needed for comparison to full-scale numerical simulations of the impact event.

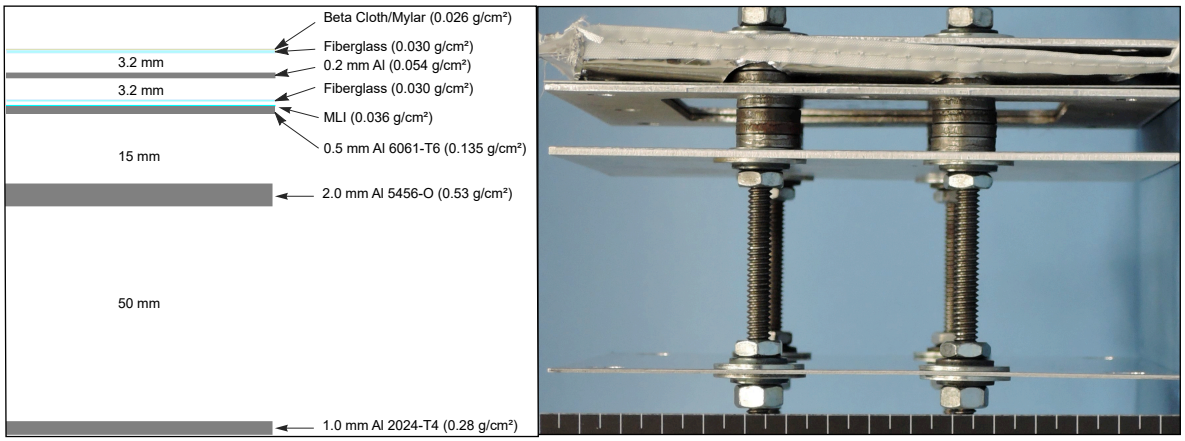

Figure 2. Representative Whipple shield with external thermal blanket (left) shield configuration schematic (layers scaled by mass; separations to scale), and (right) profile image of representative experimental article.

To this end, the Hypervelocity Impact Technology group at the NASA Johnson Space

continued on page 5

Impact Capabilities

continued from page 4

Center in Houston, Texas, and the Remote Hypervelocity Test Laboratory at the NASA White Sands Test Facility in Las Cruces, New Mexico, teamed up to obtain 11 representative impacts of cylindrical CFRP projectiles at about seven kilometers per second into the shield shown in Figure 2 [9]. These experiments performed two functions: first, they allowed the development of manufacturing techniques, launch conditions, and diagnostic techniques necessary to achieve ballistic data for cylindrical projectiles at orbital speeds, and second, they provided data for comparison to numerical simulations for the popular Whipple shield system. The cylindrical projectiles fell into three general categories: "flake-like," with ratio of length (L) to diameter (D), L:D, of *approximately* 1:3, where a representative example is shown in Figure 3 (left-hand side), spherical mass-equivalent with L:D of 2:3 shown in Figure 3 (center), and "needle-like" with an L:D ratio of 3:1 shown in Figure 3 (right-hand side).

The projectiles have been fabricated from both axially extruded Torayca® T700 fiber systems in a rod-stock form with a high-performance Bisphenol A epoxy resin binder [10], and a plane-woven, 1/16 inch-thick, sheet-stock of Ultra-Strength, Lightweight Carbon Fiber [11]. The projectile geometry for the "needle-like" and spherical mass-equivalent projectiles are determined by the initial diameter of the parent rod-stock material and are cut to length with a rotating very-fine-grit, diamond-cutoff wheel mounted on the tail stock of a counter-rotating lathe. The projectile geometry for the "flake-like" projectiles is derived from the sheet-stock material and is cut with a high-pressure, water-jet cutter to the required diameter. All projectile dimensions are characterized using a Keyence VHX-5000 Digital Microscope with VH-Z20R objective to a 25 µm resolution. All three projectile geometries are accelerated within a separable sabot by a 0.50 caliber, two-stage, light-gas gun with the cylindrical axis of the projectile in the direction of the barrel.

While all projectiles are accelerated with their cylindrical axis pointed toward the target, the release from the carrying sabot and the flight within the target chamber results in the potential for an arbitrary rotation of the projectile. To address this potential rotation, two frame-synchronized Shimadzu HyperVision HPV-X cameras with Nikon AF Zoom-NIKKOR 80-200 mm Extra-low Dispersion lenses image the projectile at 2 million frames per second as the projectile approaches the target. For maximum light collection, the objective lenses have been set at f/2.8. These two cameras are placed orthogonal to each other outside of the target chamber as seen in Figure 4 (left-hand image).

The cameras, located 45° down from the top of the target chamber, are focused on an alignment fixture (Figure 4, top, right-hand image)

continued on page 6

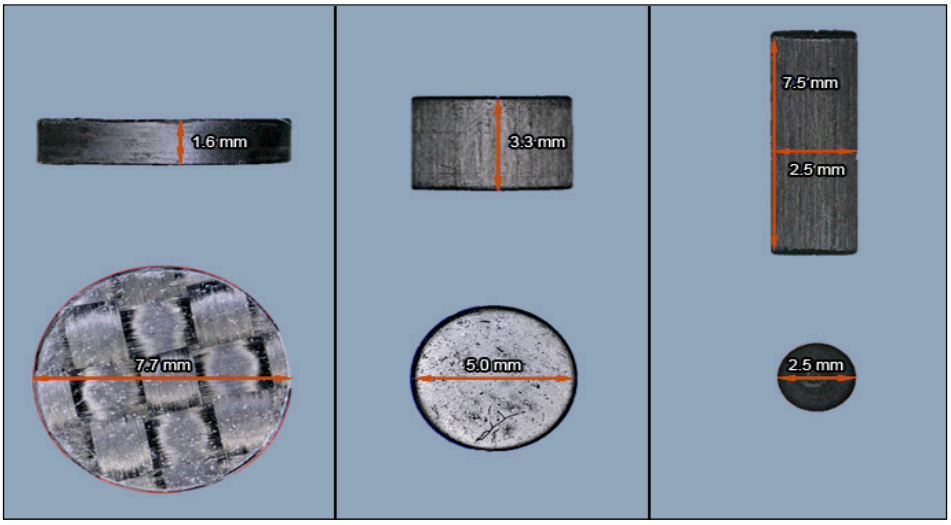

Figure 3. Side and top images of representative cylindrical, CFRP projectiles for (left-hand) "flake-like" at L:D~1:3 (actual L:D range of 1:2.5-1:5, determined by fixed thickness of stock material and variable diameter; L:D = 1:4.8 in this case); (center) spherical mass-equivalent at L:D=2:3; and (right-hand) "needle-like" at L:D=3:1.

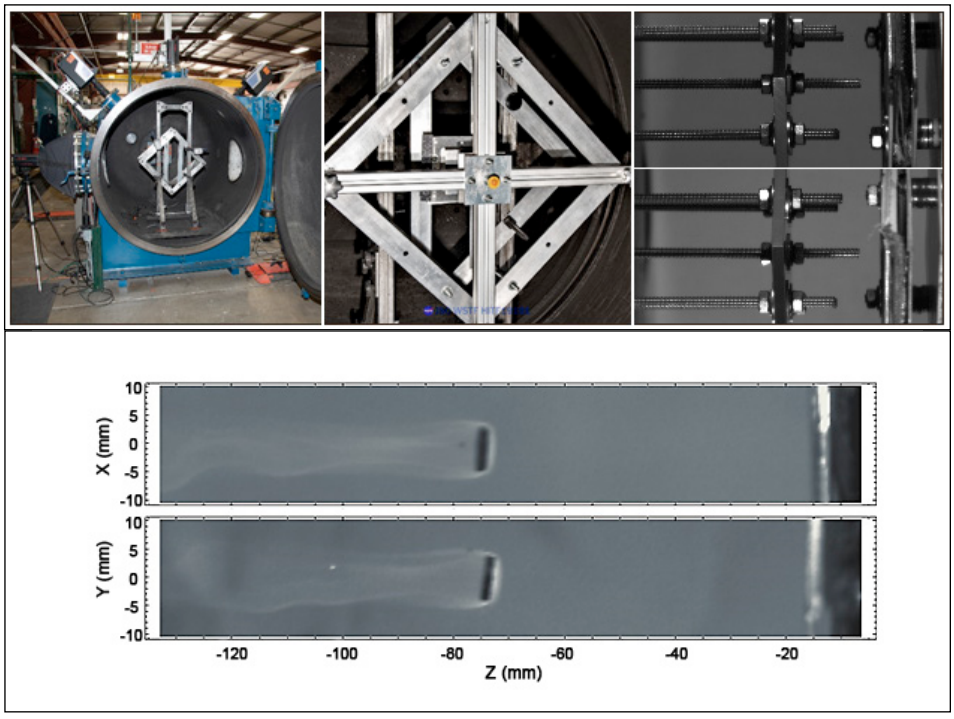

Figure 4. (top images) Pre-impact imagery of the projectile relies on a pair of frame-synchronized, ultrahigh-speed Shimadzu HyperVision HPV X cameras located outside the target chamber (left-hand image) to image the target (center image, the dual attachment fixture in detail). The cameras are aligned orthogonal to each other and focused on the flight path of the projectile prior to each shot by an in situ alignment tool consisting of five, precisely located, all-thread rods (right-hand image). The two, 2 million-frame-per-second cameras are capable of capturing about 40 frames of the projectiles moving at 7 km/s as they move toward the target over their field of view.
(bottom image) These images of the projectile just prior to the moment of impact enable the calculation of the orientation of the projectile with respect to its velocity vector. In these backlit images, the shadow of the projectile is about 10 µs from the target on the far right and the visible radiation from the bow shock wave generated by the projectile is also visible in the image.

Impact Capabilities

continued from page 5

that is placed immediately in front of the target. The alignment fixture provides a reference to adjust the cameras so that they are orthogonal, has features for focus adjustment at the expected flight path, and provides a spatial absolute reference for scaling the camera images at the expected position of the projectile in flight.

A secondary target frame, also shown in Figure 4 (top, center image), directly interfaces with the target chamber and holds the primary target of Figure 2 and alignment tool for each shot. This dual frame approach allows the rapid and repeatable change-out of targets between successive shots without altering the camera alignment. The secondary target frame also provides background screens to each of the Shimadzu cameras.

These background screens reflect the light from the illumination source at the top of the target chamber directly back to the cameras, allowing an approximately flat backlighting of the projectile as it approaches the primary target, as shown in the scaled images of Figure 4 (bottom image). From these two orthogonal views, angles between the cylinder's axis and the velocity vector can be measured for each view. These orthogonal rotation angles can then be used to calculate the true angle between the cylinder axis and velocity vector, which cannot be measured unambiguously in either of the views.

In all, 11 impact experiments with CFRP cylinders have been performed for this version of the Whipple shield with its external thermal blanket [8]. In these impact experiments, all of the projectile velocities have been in the range of 6 to 7 kilometers per second and have been launched perpendicular to the target. The collected records have varied length-to-diameter ratios of the cylindrical projectiles, and by the variability of each launch, the orientation at impact has also been varied. The projectile dimensions have been selected by predictive simulations from the model in Reference 7 to bracket the ballistic limit of the shield to initiate this effort.

As the goal of these experiments is to develop a database of validation data to compare to numerical simulations, a representative comparison from the observed damage in the 2.0 mm-Al5456-O rear wall for an L:D of 1:4.8 is compared to the result from the simulation in Figure 5 (top left). The experimental record is shown in the left-hand image, and the corresponding simulation is shown in the right-hand image. The L:D of 1:4.8 shot used a cylindrical CFRP projectile with a nominal diameter and length of 7.7 mm and 1.6 mm, respectively. The CFRP projectile's axis tilted away from the velocity vector in flight by 9.1°, and the impact perforated the rear wall of the Whipple shield.

Next to the experimental record is a density contour showing the same viewpoint from a numerical simulation that used the initial impact parameters from the experiment. The two images are approximately at the same scale. As can be seen in the experimental image and the simulation contour, the simulation accurately reproduced the approximately 1.5 cm-width hole; although, at 30 µs after impact when this density contour was captured, some of the spalled aluminum material is still in view at the center of the hole as it moves away from the rear wall.

In contrast, the L:D of 1:2.5 shot shown in Figure 5 (bottom left) used a cylindrical CFRP projectile from the same sheet-stock, but the diameter has been reduced to 4.0 mm. This smaller projectile impacted with its cylindrical axis rotated 14.9° from the velocity vector and did not perforate the 2.0 mm-Al5456-O rear wall. The impact only produced craters in the front surface of the rear wall. This experimental record is also compared to the numerical simulation, which accurately reproduced that the rear wall would remain intact. The lighter orange region in the numerical simulation is where aluminum material is pushed out of a cell of the simulation space with each alternating lighter and darker band representing 0.3 mm of depth. The combination of these two conditions of one perforated and one intact shield wall bracket the ballistic limit.

Figure 5 (top and bottom, center images) shows similar comparisons for the experimental conditions with a cylinder length-to-diameter

continued on page 7

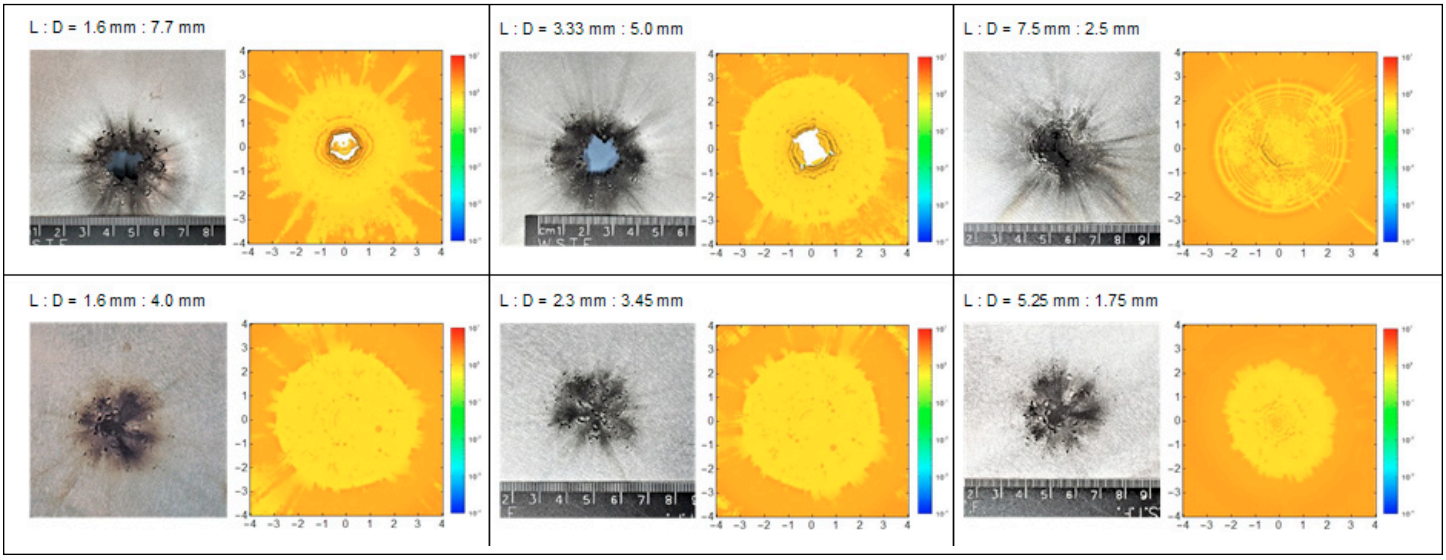

Figure 5. Comparisons of experimental observations to simulations for two "flake-like" projectiles at (top, left-hand) L:D=1:4.8 with diameter 7.7 mm and (bottom, left-hand) L:D=1:2.5 with diameter 4.0 mm; for two spherical mass-equivalent projectiles at L:D=2:3 with diameters of (top, center) 5.0 mm and (bottom, center) 3.45 mm; and for two "needle-like" projectiles at L:D=3:1 with diameters of (top, right-hand) 2.5 mm and (bottom, right-hand) 1.75 mm. In each subfigure, the grayscale images are close-up photographs of the front surface of the 2.0 mm-Al5456-O rear wall of the Whipple shield in Figure 1, and the color images are density contours of the simulated aluminum wall in the same view. The simulation model from Reference 7 accurately predicted the ballistic limit and reproduced the observed damage to the rear wall.

Impact Capabilities

continued from page 6

of 2:3. The impact result in the top, center image is from a 5.0 mm-diameter projectile that hit with the cylindrical axis rotated by 13.1° from the velocity vector, and the result in the bottom, center image is from a 3.45 mm-diameter projectile rotated at 64.2°. Similarly, in the Figure 5 right-hand images, the projectiles have a length-to-diameter of 3:1, and the diameters and rotations are 2.5 mm and 47.7°, and 1.78 mm and 81.2°, respectively.

In both length-to-diameter ratios, images are shown for a projectile that exceeds the shield's ballistic limit and for a projectile below the shield's ballistic limit, albeit, Figure 5's top, right-hand image is right on the ballistic limit with very small perforations. In the case of all three length-to-diameter ratios, the comparison between the experimental observation and numerical simulation are good, lending confidence in using simulations to extrapolate to other impact conditions as was done in Reference 7.

As can be seen through this effort, significant progress has been made in developing techniques to validate constitutive, material models for numerical simulation on non-spherical projectile impacts. First steps have been made to develop techniques to manufacture, accelerate to orbital speeds, and diagnose the orientation at impact for projectiles representative of the collected debris from the DebriSat experiment. The initial experiments demonstrate good predictive capability for the numerical simulation model developed in Reference 7 for CFRP projectiles.

Future work is planned to extend to other projectile materials like aluminum, steel, and copper, and to consider other shield systems including other Whipple shields, thermal protection systems, higher density monolithic/quasi-monolithic structures, and multi-shock shields. The combined effort of experimental validation and numerical modeling are intended to develop confidence in broad-ranging, ballistic-limit equations for non-spherical projectiles in preparation for future Bumper implementation of ORDEM 4.0 to improve orbital debris impact risk assessments for spacecraft design reliability and survivability.

References

1. Polk, M., *et. al.* "Orbital debris assessment testing in the AEDC Range G," *Procedia Engineering*, 103, pp. 490-498 (2015).

2. Liou, J.-C., *et al.* "Successful Hypervelocity Impacts of DebrisLV and DebriSat," *Orbital Debris Quarterly News*, vol. 18, issue 3, pp. 3-5, (2014).

3. Liou, J.-C., *et. al.* "DebriSat-A planned laboratory-based satellite impact experiment for breakup fragment characterization," *International Astronautic Congress Proceedings*, IAC-16.A6.2.8x35593 (2016).

4. Fitz-Coy, N., *et. al.* "Characterization of debris from the DebriSat hypervelocity test," 66th International Astronautical Congress at Jerusalem, Israel, IAC-15-A6.2.9x30343, pp. 1-10 (2015).

5. Christiansen, E.L. "Meteoroid/debris shielding," NASA/TP-2003-210788 (2003).

6. Whipple, F.L. "Meteorites and space travel," *Astronomical Journal*, 52:1161, 131 (1947).

7. Miller, J.E., *et al.* "Analytic ballistic performance model of Whipple shields," *Procedia Engineering*, 103, pp. 389-397 (2015).

8. Miller, J.E. "Implication of debris fragment shape on shield protection capability," *Orbital Debris Quarterly News*, vol. 22, issue 4, pp. 2-4, (2018).

9. McCandless, R.J., Davis, B.A. and Miller, J.E. "Carbon fiber reinforced polymer shape effect hypervelocity impact test program," NASA Johnson Space Center Report, JSC-67500, (2020).

10. CST The Composites Store, Inc. "Comparison Data for Pultruded Shapes," http://www.cstsales.com/rod_comp.html. Accessed 2 June 2020.

11. McMaster-Carr. "Ultra-Strength Lightweight Carbon Fiber Sheet,". https://www.mcmaster.com/8181K14. Accessed 2 June 2020.

♦

PROJECT REVIEW

Short-Term Satellite Breakup Risk Assessment Model Process

D. GATES AND M. MATNEY

Space operations over the past 63 years have resulted in more than 250 fragmentation events. While the long-term characterization of the orbital debris environment is of primary importance for space sustainability, there is also a need to assess the immediate risk to spacecraft following a fragmentation event on the scale of hours to days. To address this, the Orbital Debris Program Office (ODPO) developed the in-house Satellite Breakup Risk Assessment Model (SBRAM) [1, 2].

The original version of SBRAM was created more than two decades ago and has been used to analyze risks to the International Space Station (ISS) and Shuttle missions; however, it can be used to evaluate the short-term risk to any orbiting asset. Recently, a number of changes and upgrades have been added to improve its capability. Here we will discuss the fundamentals of how the model works, describe the upgrades, and provide an example of its capabilities.

A number of models have been created to assess the short-term hazard to satellites from a recent breakup in space. Much of the work has been of a semi-analytic nature, describing the evolution of a debris cloud in terms of probability distributions. Theoretical work by Chobotov [3], Spencer [4], McKnight [5], and Jehn [6] have sought to describe a breakup cloud as analytical continuum distributions. However, these methods do not model well the important orbit perturbation effects (such as drag and solar radiation pressure) that can drive the risk from small debris. The method adopted for SBRAM is to avoid analytic descriptions of the growth of the debris cloud, employing instead a Monte Carlo analysis

continued on page 8

SBRAM Process

continued from page 7

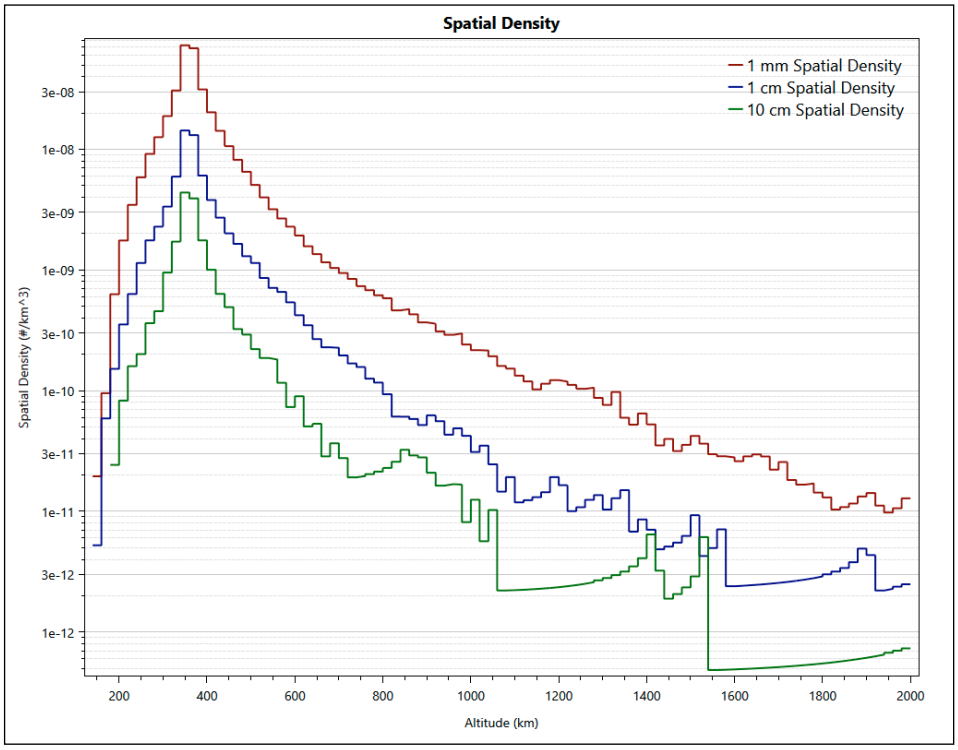

Figure 1. Spatial density distributions of ≥1 mm, ≥1 cm, and ≥10 cm debris from a simulated explosion in SBRAM.

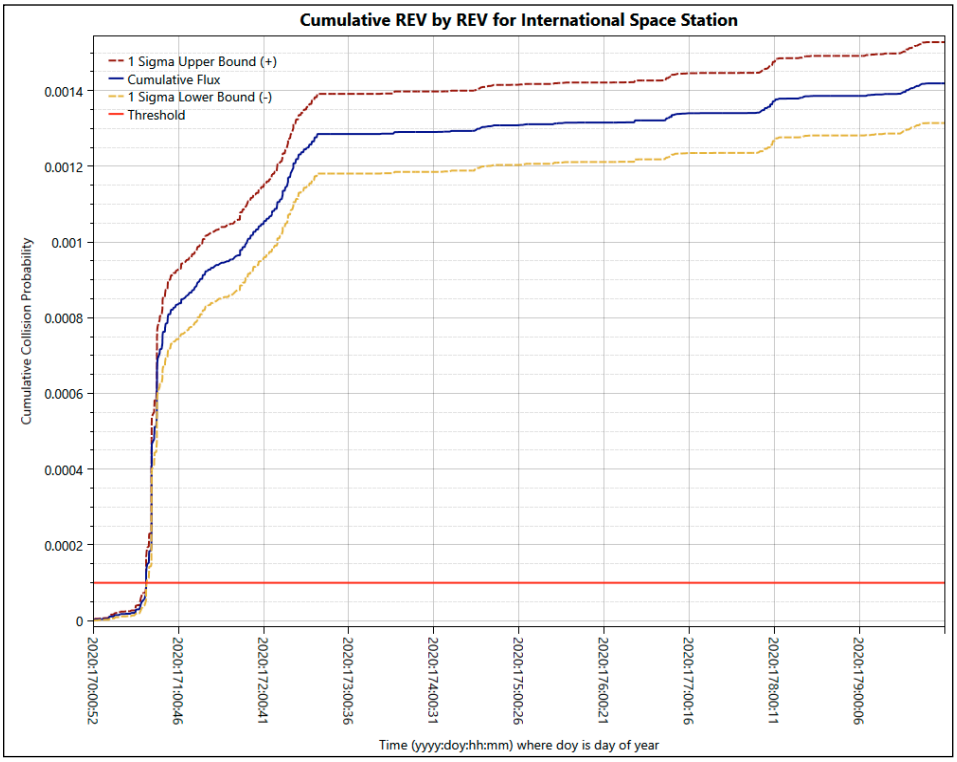

Figure 2. Cumulative revolution-by-revolution collision probability of the debris from a simulated explosion with the International Space Station over 10 days. The "Threshold" value refers to a user-defined value at which the asset is at significant risk. The user-defined 10^{-4} threshold line here is red because the cumulative flux on the ISS has exceeded the threshold. This indicates that the risk to the asset from the debris generated by the explosion is unacceptable and further risk mitigation actions may be warranted.

of individual orbits where all appropriate perturbation equations are incorporated in the propagation. The aggregate probability is computed using a modified Gaussian mixture method.

SBRAM simulates a discrete cloud of debris using the NASA Standard Satellite Breakup Model (SSBM) [7] and propagates the debris particles deterministically under perturbations from solar radiation pressure, atmospheric drag, Earth gravitational harmonics, and lunar and solar gravity. The risk to an asset object is computed by determining close approaches between each randomly-created debris piece from the SSBM and the asset object. The actual collision probability is computed using a generic, modeled probability distribution centered on each of the bodies within their respective orbits and comparing details of their close-approach geometry. In addition to computing the probability of collision, the software preserves information on the size of the debris, the estimated time and location within the asset's orbit of the close approach, and from what directions the debris threatens the asset.

In general, the collision risk is sensitive to the initial distributions in the discrete breakup debris cloud, so the model is set up to run multiple, random cloud cases to compute reasonable average collision rates. This consists of using the breakup model to create a cloud of particles and then assigning them delta-velocity magnitudes (based on the SSBM distributions) and random directions. These velocities are then added to the parent object's velocity to produce the final, post-event, velocity vector. Each fragment is also assigned an area-to-mass ratio based on the SSBM.

These particles are then propagated in time and close approaches to the asset are identified (within certain user-defined minimum criteria). The circumstances of each such conjunction are computed – time, miss distance, and the position and velocity state vectors of the asset and debris. From this information, the probability of collision is computed and summed over all possible conjunctions. Then, a new random cloud is generated, the particles are propagated in time, and the collision probabilities are recomputed. This procedure is repeated for each Monte Carlo step, and the total probability is averaged over the Monte Carlo ensemble.

Once a conjunction is identified, the information must be transformed into a collision probability. To make this calculation tractable, SBRAM uses "position-uncertainty ellipsoids"

continued on page 9

SBRAM Process

continued from page 8

similar to those used by the Shuttle and ISS conjunction assessment models to compute probability of collision and identify collision avoidance maneuvers.

SBRAM assigns each debris object a 3-dimensional, Gaussian, prolate-probability-distribution ellipsoid with the major axis aligned with the velocity vector. Instead of using these ellipsoids to predict conjunctions of actual objects, SBRAM uses them as spatial density distributions, with the idea that the superposition of many such small Gaussians will approximately "map out" the composite probability distribution of a large breakup cloud.

For most conjunctions, SBRAM uses a linear approximation to compute the encounter between a modeled debris object and an asset. This assumes that the path of the high velocity encounter can be approximated as linear, which allows for simplification of the mathematics involved and speeding up of the computation time. However, for certain low-velocity conjunction geometries (which typically occur when the orbits of the debris and asset are nearly coplanar) this linear approximation can result in computational problems in finding the close approach, as well as errors in the probability calculation.

For the SBRAM update, we have included logic to handle such low-velocity encounters, using an explicit numerical time integration algorithm to calculate the collision probability. We have also updated the model's ability to assess the debris risk from catastrophic collisions between space objects and improved the propagator logic to handle ballistic orbits (to compute the risk from the short-lived cloud). The graphical user interface (GUI) has been completely redesigned to improve the usability of the model.

A common ODPO application for SBRAM is assessing the risk to human spaceflight assets. As a demonstration of the model's capabilities, we assess the risk to the ISS shortly after two simulated on-orbit events: a rocket body exploding and a collision between spacecraft.

The first scenario was modeled in an orbit with an apogee altitude of 458.7 km, a perigee altitude of 447.8 km, and an inclination of 128.4°. The collision probability of any fragment that can damage the ISS was calculated for 10 days after the event. Note, the orbit was chosen to be a "worst case" scenario for illustrative purposes only, because the inclination of the ISS (51.6°) and that of the debris add up to 180°.

continued on page 10

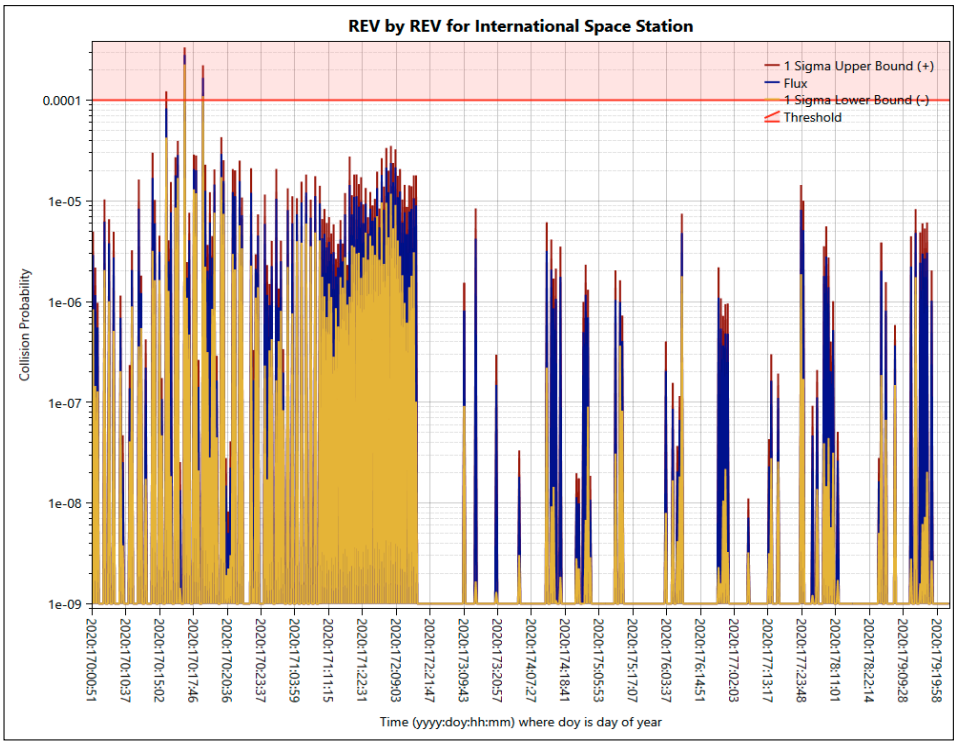

Figure 3. Revolution- by-revolution collision probability of the debris from the simulated explosion with the ISS over 10 days. The "Threshold" value refers to a user-defined value at which the asset is at significant risk. It is red in this case because at least one mean flux value exceeded the threshold. The red lines above each blue spike represent the 1-sigma uncertainty in that flux value, averaged over all the Monte Carlo simulations. The corresponding yellow line denotes the lower 1-sigma bound, again averaged over all the Monte Carlo simulations. Note that the risk is not constant in time, but changes as the debris cloud evolves and the orbits precess relative to one another. As a result, there are time windows with enhanced risk, and other windows where there is temporarily no risk from this debris cloud.

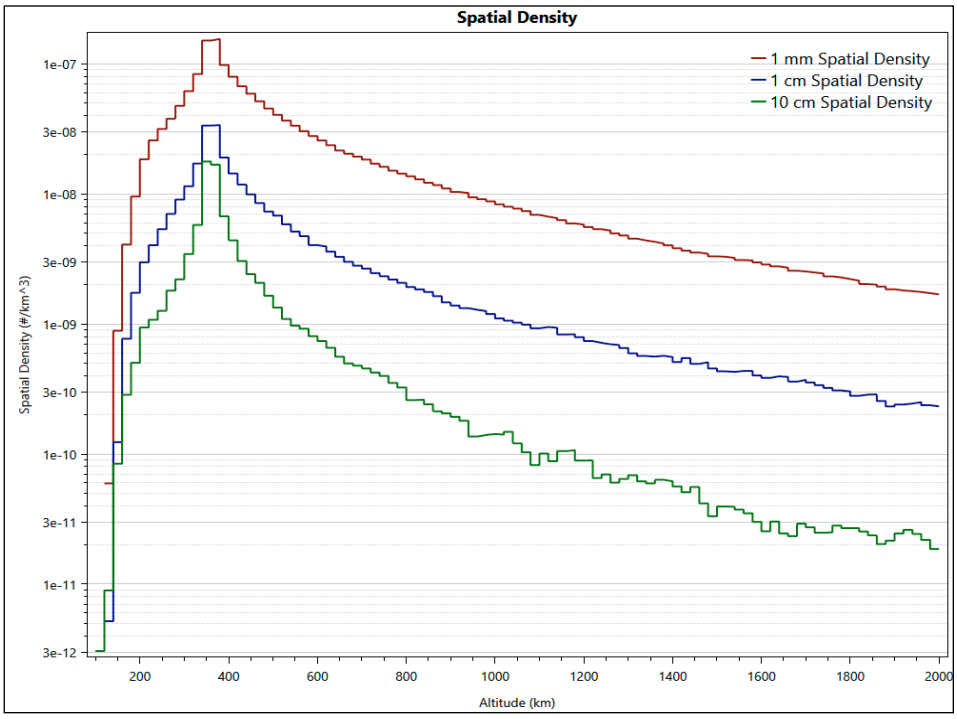

Figure 4. Spatial density distributions of ≥1 mm, ≥1 cm, and ≥10 cm debris from the simulated collision in SBRAM.

SBRAM Process

continued from page 9

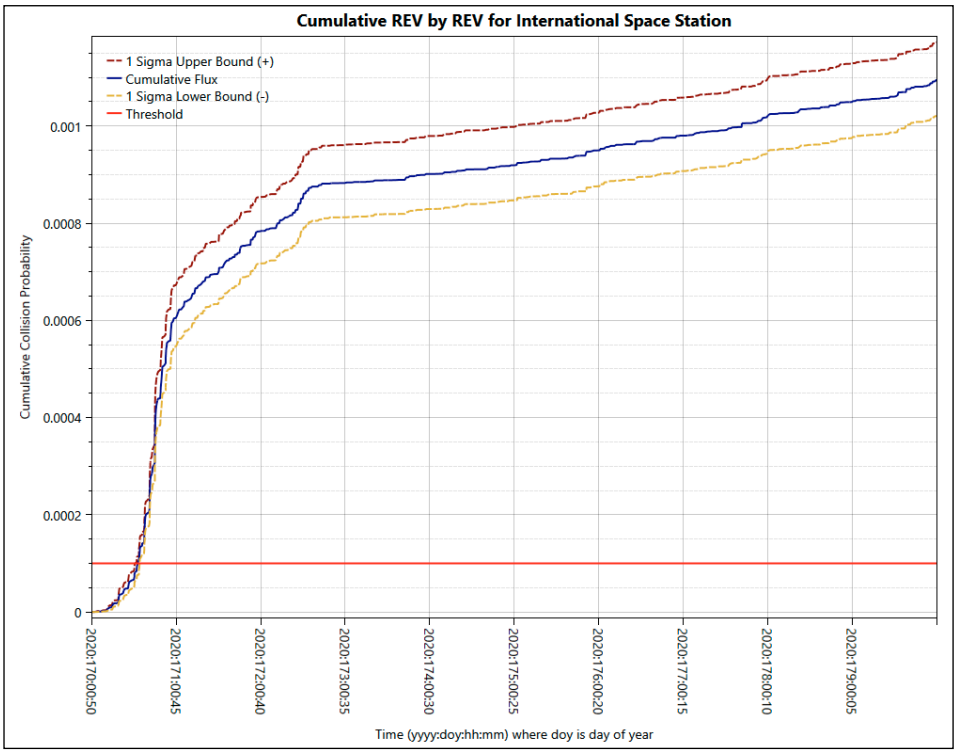

Figure 5. Cumulative revolution-by-revolution collision probability of the debris from the simulated collision with the ISS over 10 days. The "Threshold" value refers to a user-defined value at which the asset is at significant risk. The user-defined 10^{-4} threshold line is red because the cumulative flux on the ISS has exceeded the threshold. This indicates that the risk to the asset from the debris generated by the collision is unacceptable and a subsequent maneuver may be warranted.

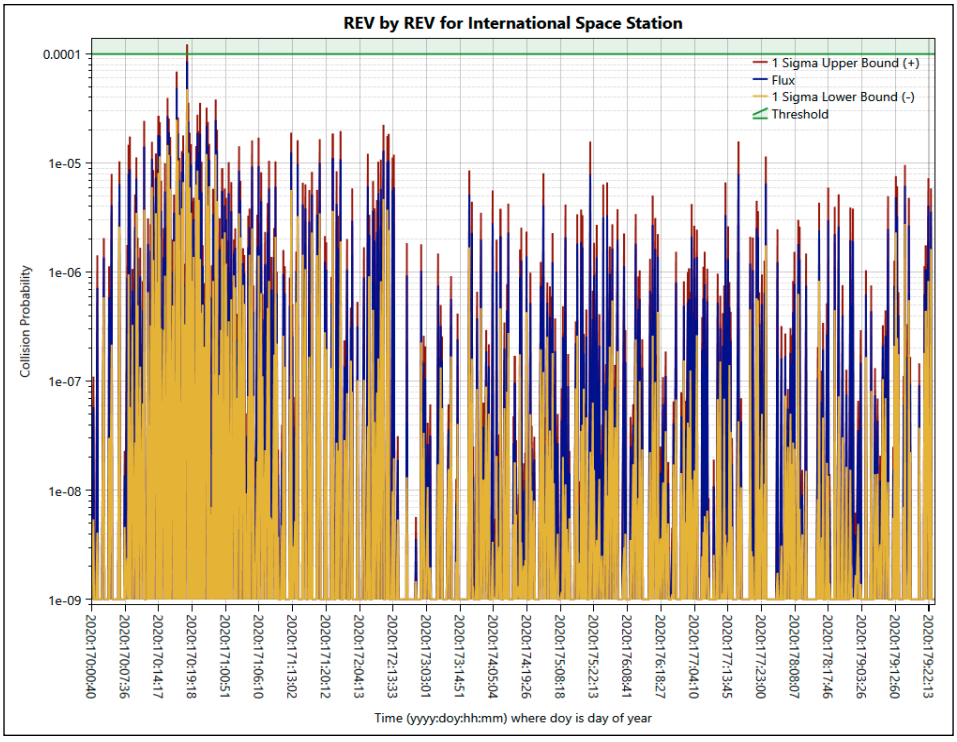

Figure 6. Revolution-by-revolution collision probability of the debris from the simulated collision with the ISS over 10 days. The "Threshold" probability here refers to a user- defined value (10^{-4}) at which the asset is at significant risk. It is green in the above chart because no mean flux value exceeded the threshold—though, note that at least one value of mean flux + 1 sigma uncertainty exceeds the threshold. What is shown is the composite risk from the two independent collision clouds, each evolving separately over time.

Figure 1 shows the spatial density of this hypothetical breakup event, which is used to analyze the distribution of fragments generated by the modeled event. Figure 2 shows the asset's cumulative orbital revolution-by-revolution probability that any fragments from the breakup event collided with the ISS, and Figure 3 shows the differential probability of collision with the ISS on a revolution-by-revolution basis.

The second scenario was modeled such that two spacecraft collided in orbits with an apogee altitude of 458.7 km, a perigee altitude of 447.8 km, and inclinations of 128.4° and 51.6°, respectively. The first spacecraft was given a mass of 600 kg and the second spacecraft a mass of 900 kg. The collision probability of any fragment that could damage the ISS was calculated for 10 days after the event.

Figure 4 shows the spatial density of the breakup event, which is used to analyze the distribution of fragments generated by the modeled event. Figure 5 displays the cumulative revolution-by-revolution probability that any fragments from the breakup event collided with the ISS, and Figure 6 shows the differential probability of collision with the ISS on a revolution-by-revolution basis.

In conclusion, SBRAM has undergone a significant upgrade that allows the user to customize breakup clouds, handles low-velocity, coplanar flux and ballistic fragments, and allows the user to analyze the risk posed to an asset from the debris generated by on-orbit collisions and explosions immediately following the event.

In contrast to the publicly-available ODPO Orbital Debris Engineering Model, which allows a user to predict the total flux their spacecraft would expect to experience from orbital debris over its lifetime, SBRAM is designed for dynamic scenarios immediately following a breakup to determine whether or not specific corrective measures are required in response to a collision or explosion on orbit.

References

1. Matney, M. "The Satellite Breakup Risk Assessment Model," *Orbital Debris Quarterly News*, vol. 3, issue 3, pg. 7, (July 1998).

2. Krisko, P., *et al.* "SBRAM Upgrade to Version 2.0," *Orbital Debris Quarterly News*, vol. 9, issue 3, pp. 2, 9 (July 2005).

3. Chobotov, V.A., and Spencer, D.B. "Debris Evolution and Lifetime Following an Orbital Breakup," *Journal of Spacecraft and Rockets*, vol. 28, issue 6, pp. 670-676, (1991).

continued on page 11

SBRAM Process

continued from page 10

4. Spencer, D.B. "The Effects of Eccentricity on the Evolution of an Orbiting Debris Cloud," *Advances in Astronautical Sciences*, vol. 65, Pt. 1, pp. 791-807, (1987).

5. McKnight, D.S. "A Phased Approach to Collision Hazard Analysis," *Advances in Space Research*, vol. 10, issue 3, pp. 385-388, (1990).

6. Jehn, R. "Dispersion of Debris Clouds from In-Orbit Fragmentation Events," *ESA Journal*, vol. 15, issue 1, pp. 63-77, (1991).

7. Johnson, N.L., *et al*. "NASA's new breakup model of evolve 4.0," *Advances in Space Research*, vol 28, issue 9, pp 1377-1384, (2001).

8. Bromiley, P.A. "Products and Convolutions of Gaussian Probability Density Functions," University of Manchester, School of Health Sciences, Division of Informatics, Manchester, UK, Tina Memo No. 2003-003 Internal Report, pdfs.semanticscholar.org, (2003). ♦

Two Recent Breakup Events Updated

Three breakups were reported in the previous issue (ODQN, vol. 24, issue 2, pp. 12). This brief note updates the readership on two of the events, namely those associated with Cosmos 2535 and the Meteor 3-5 *Tsyklon 3* rocket body. Readers are directed to the referenced ODQN issue for fundamental details of each mission and the specific events themselves.

The Cosmos 2535 (International Designator 2019-039A, U.S. Space Command [USSPACECOM] Space Surveillance Network [SSN] catalog number 44421) spacecraft fragmented at approximately 22:00 GMT on 9 January 2020 after a half-year on orbit. In addition to the Cosmos 2535 payload, a total of 17 additional debris (piece tags Q-AG inclusive) is associated with the 9 January event as of 4 July 2020. Nine have decayed from orbit while the parent body and 8 additional debris remain on orbit. These are illustrated in the figure's Gabbard diagram. Spacecraft configuration, stored energy, and event root cause remain unknown.

The Meteor 3-5 rocket body (International Designator 1991-056B, SSN# 21656), an SL-14/*Tsyklon 3* upper stage and S5M third stage, fragmented at 10:46 GMT on 12 February 2020, after over 28 years on-orbit. As of 5 March 2020, and in addition to the parent body, 61 debris (piece tags C-BQ inclusive) had entered the satellite catalog. As of 4 July, the associated debris had increased to 93 pieces (through piece tag CZ). All remain on-orbit. ♦

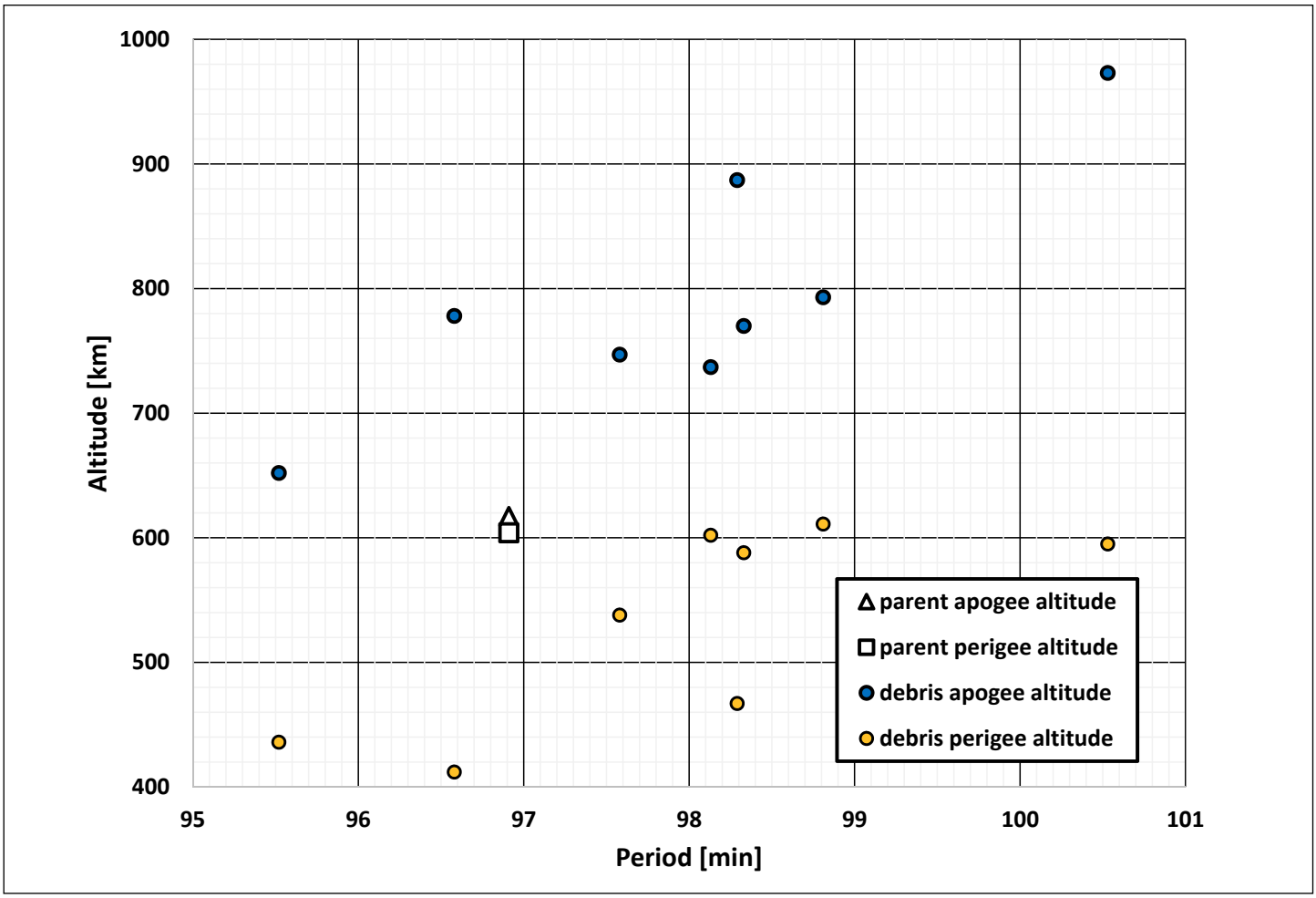

A Gabbard diagram of the 9 January 2020 2019-039 event. Approximate epoch is 4 July 2020.

UPCOMING MEETINGS

These events could be canceled or rescheduled due to the COVID-19 pandemic.
All information is current at the time of publication.
Please consult the respective websites for updated schedule changes.

Canceled: 17th Annual Cubesat Developer's Workshop, San Luis Obispo, CA, USA

Due to the worldwide COVID-19 pandemic, the 2020 meeting was canceled and will reconvene in April 2021. However, select papers and presentations that had been collected for the 2020 workshop are available at the workshop website: https://www.cubesat.org/workshop-information .

1-6 August 2020: Virtually Amazing—the 34th Annual Small Satellite Conference

Utah State University (USU) and the AIAA will sponsor the 34th Annual AIAA/USU Conference on Small Satellites in a virtual format, with content being uploaded daily over the course of the conference. This year's theme is "Space Mission Architectures: Infinite Possibilities," and will explore the realm of space mission architectures and how these may support the diverse needs of the global space community. Conference information is available on the organizer's website at https://smallsat.org/.

15-18 September 2020: All-Virtual 21st Advanced Maui Optical and Space Surveillance Technologies Conference

The technical program of the 21st Advanced Maui Optical and Space Surveillance Technologies Conference (AMOS) will focus on subjects that are mission critical to Space Situational Awareness. The technical sessions include papers and posters on Orbital Debris, Space Situational/Space Domain Awareness, Adaptive Optics & Imaging, Astrodynamics, Non-resolved Object Characterization, and related topics. The abstract submission deadline passed on 1 March 2020. Additional information about the conference is available at https://amostech.com .

12-14 October 2020: 71st International Astronautical Congress (IAC)—The Cyberspace Edition

The IAC will convene virtually in 2020 with a theme of "Inspire, Innovate & Discover, for the Benefit of Humankind." The abstract submission closed on 28 February 2020. Registration is required, but is free, and content will consist of both live and pre-recorded sessions. Additional information for the 2020 IAC is available at http://www.iafastro.org/events/iac/iac-2020/ and http://iac2020.org/ . Dubai, United Arab Emirates, the 2020 host, will now host the 2021 72nd IAC from 25-29 October 2021.

2 December 2020: 5th Space Debris Re-entry Workshop, Darmstadt, Germany

The European Space Operations Centre (ESOC) will host the 5th Space Debris Re-entry Workshop in December 2020. The workshop aims to address the side effects of the increased traffic to orbit, which triggered a renewed interest in the practicalities of having objects, large and small, re-entering uncontrolled after the end of mission. The symposium style for the past events transitions this year to a workshop around the open problems burgeoning by the increase in uncontrolled re-entry "traffic": how to transition from uncertainty assessment to operational products when it comes to re-entry predictions and orbital lifetimes? Which multi-physics driven break-up processes produce predictions which can be verified on a macroscopic level to cause first fragmentation? The submission of abstracts on those questions is encouraged, but the venue is open to other topics related to general orbital lifetime estimation, re-entry predictions on catalogue level, low thermosphere orbit observations and orbit determination, and material and aerothermal responses of re-entering objects in the continuum regime. Among the objectives of the workshop are linking space surveillance, astrodynamics, and re-entry physics to cover all aspects of the problem. The abstract and registration deadline dates are 12 October and 9 November 2020, respectively. Detailed information is available at https://reentry.esoc.esa.int/home/workshop .

14-16 December 2020: 6th International Workshop on Space Debris Modeling and Remediation, Paris, France

CNES Headquarters will host the 6th International Workshop on Space Debris Modeling and Remediation. Topics are anticipated to include, but are not necessarily limited to modeling, including specificities coming from small satellites and constellations; high level actions and road-maps associated to debris remediation; remediation system studies, including those relative to small debris; design of specific concepts, including new ideas relative to just-in-time collision avoidance and proposals devoted to large constellations and small satellites; concepts derived from current space tugs initiatives; GNC aspects, rendezvous sensors and algorithms, de-spin, control during de-boost; and policy, economics, insurance, intellectual property, national security, and international cooperation aspects of debris remediation. Workshop attendance is limited to 130. The abstract submission deadline is 14 September 2020, and additional details regarding the process are available from Mr. Christophe Bonnal at Christophe.bonnal@cnes.fr.

continued on page 9

UPCOMING MEETINGS - Continued

continued from page 12

28 January-4 February 2021: COSPAR 2021, Sydney, Australia

Due to the worldwide COVID-19 pandemic, the 43rd Assembly of the Committee on Space Research (COSPAR) Scientific will convene in the Sydney International Convention Center in early 2021, rather than August 2020, as COSPAR 2021. The COSPAR panel Potentially Environmentally Detrimental Activities in Space (PEDAS) will conduct a program entitled "The Science of Human-Made Objects in Orbit: Space Debris and Sustainable Use of Space." PEDAS.1 sessions will include advances in ground- and space-based measurements of the orbital debris environment, micrometeoroid and orbital debris environment modeling, end-of-life concepts, and solutions to fundamental operational challenges. The abstract submission period closed on 14 February 2020. Please see the COSPAR PEDAS.1 session website at https://www.cospar-assembly.org/admin/session_cospar.php?session=953 and the Assembly website https://www.cospar2020.org/ for further information.

5-11 June 2021: 33rd International Symposium on Space Technology and Science, Beppu, Ōita Prefecture, Japan

The 33rd ISTS will be convened in June 2021; the ODQN will provide additional Symposium details in future issues as they become available. Online abstract submission opens on 3 August 2020. Additional information about the conference is available at https://www.jsass.or.jp/webe/ .

24-29 October 2021: 16th Hypervelocity Impact Symposium, Alexandria, Virginia, USA

The Hypervelocity Impact Symposium (HVIS) is a biennial event organized by the Hypervelocity Impact Society that serves as the principal forum for the discussion, interchange, and presentation of the physics of high- and hypervelocity impact and related technical areas. The HVIS Symposia have a long-standing international reputation as a catalyst for stimulating research in this area through a wealth of oral and poster presentations, and commercial exhibits. The Symposium's proceedings are the major archival source of papers published in this field. Topics of interest to the debris community include fracture and fragmentation; meteoroid and debris shielding and failure analysis; hypervelocity phenomenology studies, launchers, and penetration mechanics and target response. The symposium's abstract deadline is 12 October 2020. Additional information for the 16th Symposium is available at http://hvis2021.jhuapl.edu/.

26-28 October 2021: 11th International Association for the Advancement of Space Safety (IAASS) Conference, Osaka, Japan

The 11th conference of the IAASS, organized in concert with the Japan Aerospace Exploration Agency, has as its theme "Managing Risk in Space." Major debris-related topics include designing safety into space vehicles, space debris mitigation and remediation, re-entry safety, nuclear safety for space missions, safety risk management and probabilistic risk assessment, and launch and in-orbit collision risk. The conference's abstract submission deadline will close on 30 April 2021. Additional information for the 2021 IAASS is available at http://iaassconference2021.space-safety.org/ .

DAS 3.1 NOTICE

Attention DAS Users: DAS 3.0.1 has been updated to DAS 3.1. DAS 3.1 is optimized for Microsoft Windows 7/8/10. Previous versions of DAS should no longer be used. NASA regulations require that a Software Usage Agreement must be obtained to acquire DAS 3.1.

To begin the process, click on the **Request Now!** button in the NASA Software Catalog at https://software.nasa.gov/software/MSC-26690-1. Users who have already completed the software request process for earlier versions of DAS 3.x do not need to reapply for DAS 3.1. Simply go to your existing account on the NASA Software portal and download the latest installer.

An updated solar flux table can be downloaded for use with DAS 3.1.

SATELLITE BOX SCORE

(as of 30 June 2020, cataloged by the U.S. SPACE SURVEILLANCE NETWORK)

Country/ Organization	Spacecraft*	Spent Rocket Bodies & Debris	Total
CHINA	411	3721	4132
CIS	1542	5357	6899
ESA	92	58	150
FRANCE	69	508	577
INDIA	100	125	225
JAPAN	187	114	301
USA	2399	4897	7296
OTHER	1048	126	1174
TOTAL	5848	14906	20754

** active and defunct*

Visit the NASA
Orbital Debris Program Office Website

www.orbitaldebris.jsc.nasa.gov

Technical Editor
Phillip Anz-Meador, Ph.D.

Managing Editor
Debi Shoots

Correspondence can be sent to:

J.D. Harrington
j.d.harrington@nasa.gov

or to:

Noah Michelsohn
noah.j.michelsohn@nasa.gov

National Aeronautics and Space Administration
Lyndon B. Johnson Space Center
2101 NASA Parkway
Houston, TX 77058

www.nasa.gov
https://orbitaldebris.jsc.nasa.gov/

INTERNATIONAL SPACE MISSIONS

01 March – 31 May 2020

Intl.* Designator	Spacecraft	Country/ Organization	Perigee Alt. (KM)	Apogee Alt. (KM)	Incli. (DEG)	Addnl. SC	Earth Orbital R/B	Other Cat. Debris
1998-067	ISS Dispensed Payloads	VARIOUS	417	420	51.6	2	0	0
2020-016A	DRAGON CRS-20	USA	408	422	51.6	0	0	2
2020-017A	BEIDOU 3 G2	CHINA	35776	35798	2.9	0	1	0
2020-018A	COSMOS 2545 (GLONASS)	RUSSIA	19112	19147	64.8	0	1	0
2020-019A	STARLINK-1279	USA	484	486	53.0	59	0	4
2020-020A	ONEWEB-0066	UK	583	614	87.6	33	0	0
2020-021A	YAOGAN-30 R	CHINA	595	602	35.0	0	1	0
2020-021B	YAOGAN-30 S	CHINA	597	600	35.0			
2020-021C	YAOGAN-30T	CHINA	590	602	35.0			
2020-022A	TDO 2 SPACECRAFT	USA	201	35460	26.5	0	1	0
2020-022B	AEHF 6 (USA 298)	USA	EN ROUTE TO GEO					
2020-023A	SOYUZ MS-16	RUSSIA	417	420	51.7	0	1	0
2019-022M	AC 10 PROBE (FULLER)	USA	453	457	51.64	0	0	0
2020-024A	NOUR 01	IRAN	420	439	59.8	0	1	0
2020-025A	STARLINK-1329	USA	549	551	53.0	59	0	4
2020-026A	PROGRESS MS-14	RUSSIA	417	420	51.7	0	1	0
2020-027A	XZF CAPSULE	CHINA	521	3044	40.9	0	1	0
2020-027B	INFLATABLE TEST MODULE	CHINA	164	367	41.1			
2020-028A	XINGYUN-2 01	CHINA	555	574	97.6	0	1	0
2020-028B	XINGYUN-2 02	CHINA	556	574	97.6			
2020-011D	ULTP	USA	476	486	51.65	0	0	0
2020-029A	USA 299	USA	NO ELEMS. AVAILABLE			0	0	0
2020-029B	USA 300	USA	NO ELEMS. AVAILABLE					
2020-030A	HTV-9	JAPAN	417	420	51.7	0	0	0
2020-031A	COSMOS 2546	RUSSIA	1689	38663	63.8	0	1	0
2020-032A	XJS G	CHINA	467	485	35.0	0	0	1
2020-032B	XJS H	CHINA	466	486	35.0			
2020-033A	CREW DRAGON DEMO-2	USA	417	420	51.7	0	0	0
2020-034A	HEAD-4	CHINA	484	502	97.3	0	0	3
2020-034B	GAOFEN 9 02	CHINA	486	504	97.3			

** Intl. = International; SC = Spacecraft; Alt. = Altitude; Incli. = Inclination; Addnl. = Additional; R/B = Rocket Bodies; Cat. = Cataloged*

The NASA Orbital Debris Photo Gallery has added high resolution, computer-generated images of objects in Earth orbit that are currently being tracked. They may be downloaded. Full instructions are at the webpage:

https://orbitaldebris.jsc.nasa.gov/photo-gallery/